

PRECISE PHOTOMETRIC TRANSIT FOLLOW-UP OBSERVATIONS OF FIVE CLOSE-IN EXOPLANETS :
UPDATE ON THEIR PHYSICAL PROPERTIES

ARITRA CHAKRABARTY^{†1,2} AND SUJAN SENGUPTA^{‡1}

¹*Indian Institute of Astrophysics, Koramangala 2nd Block, Bangalore 560034, India*

²*University of Calcutta, Salt Lake City, JD-2, Kolkata 750098, India*

(Accepted for publication in the *Astronomical Journal*)

ABSTRACT

We report the results of the high precision photometric follow-up observations of five transiting hot jupiters - WASP-33b, WASP-50b, WASP-12b, HATS-18b and HAT-P-36b. The observations are made from the 2m Himalayan Chandra Telescope at Indian Astronomical Observatory, Hanle and the 1.3m J. C. Bhattacharyya Telescope at Vainu Bappu Observatory, Kavalur. This exercise is a part of the capability testing of the two telescopes and their back-end instruments. Leveraging the large aperture of both the telescopes used, the images taken during several nights were used to produce the transit light curves with high photometric S/N (> 200) by performing differential photometry. In order to reduce the fluctuations in the transit light curves due to various sources such as stellar activity, varying sky transparency etc. we preprocessed them using wavelet denoising and applied Gaussian process correlated noise modeling technique while modeling the transit light curves. To demonstrate the efficiency of the wavelet denoising process we have also included the results without the denoising process. A state-of-the-art algorithm used for modeling the transit light curves provided the physical parameters of the planets with more precise values than reported earlier.

Keywords: techniques: photometric — stars: individual: WASP-33, WASP-50, WASP-12, HATS-18 and HAT-P-36 — planetary systems

1. INTRODUCTION

Since the discovery of the first transiting exoplanet HD 209458b (Charbonneau et al. 2000; Henry et al. 2000) it was realized that transit photometric observations are necessary to obtain a number of essential information that cannot be otherwise derived from the other methods of detection. The precise understanding on the radius, surface gravity, orbital distance, etc. helps us comprehend their formation and evolution.

Proper characterization of the already discovered exoplanets calls for repeated follow-up observations during both in-transit and out-transit epoch. In this regard the ground-based telescopes are appropriate especially in case of a transit by a close-in (hence short period) gas giant planet around a main sequence star. However, in order to observe a transient event like a transit, a coordinated set of observations around the globe will prove to be highly effective by ensuring the coverage of a transit event regardless of its ephemeris of occurrence. In this regard, the astronomical facilities of India such as Indian Astronomical Observatory (IAO, $78^{\circ} 57' E$, $32^{\circ} 46' N$), Vainu Bappu Observatory (VBO, $78^{\circ} 50' E$, $12^{\circ} 34' N$) can fill in the missing longitudinal coverage. We, therefore, observed the transit events of a few hot Jupiters using the 2m Himalayan Chandra Telescope (HCT), IAO and 1.3m Jagadish Chandra Bhattacharyya Telescope (JCBT), VBO to demonstrate the capability of these telescopes and their back-end instruments for precise

Corresponding author: Aritra Chakrabarty

[†]aritra@iiap.res.in

[‡]sujan@iiap.res.in

transit photometry. The HCT has already been a part of the detection of the planet TRAPPIST-1 b (Gillon et al. 2016). This had motivated us to continue the search and follow-up observations using HCT and JCBT. In this paper we present the transit light curves of the hot gas giants WASP-33 b, WASP-50 b, WASP-12 b, HATS-18 b and HAT-P-36 b.

Apart from the photometric noise, noise due to other sources such as stellar activity, variation in the sky transparency etc. contribute to the fluctuations in the transit light curves to a great extent which subsequently constrain the precision in determining the transit parameters. Different types of noise require different treatments. We have performed differential photometry to reduce the patterns that affect all the stars in a frame equally such as gradual variation in the airmass over the span of 3-4 hours of observation, large-scale transparency fluctuations that change the apparent brightness of all the stars in the frame almost equally etc. Also, prior to the modeling of the transit light curves, we have performed preprocessing on the light curves using the wavelet-based denoising technique. This decorrelation method suppresses the patterns of variability that are common to all the stars in the field but uncorrelated in time. These patterns can be caused by the medium-scale transparency fluctuations or seeing fluctuations that affect the stars on a frame slightly unequally but temporally uncorrelated. Also, this method removes the outliers caused by the cosmic-ray hits etc. Wavelet-based light curve noise analysis and filtering can be found in Cubillos et al. (2017); Waldmann (2014). In case of transit photometry, del Ser et al. (2018) has shown that this denoising technique does not alter the underlying astrophysical signals but improves the results obtained after modeling the transit light curves. Such preprocessing of data is a part of our self-developed pipeline used for reduction, analysis and modeling. For a comparison, we have also analysed the data without using the wavelet denoising process.

In addition to these patterns, confusing signals caused by stellar activity or pulsation are unique to each star and temporally correlated and can not be suppressed or removed by decorrelation or de-noising. They can, however, be modelled alongside the signal of interest. Such activity or pulsations have already been reported for some of the host stars (von Essen et al. 2014; Mancini et al. 2015). We have addressed to such situations by modeling the covariance structure of the confusing signal using GP regression (Johnson et al. 2015; Barclay et al. 2015), in order to ensure that their effects are accounted for properly in the posterior uncertainty estimates for the fitted parameters of the transit light curves. Photon noise, propagated through the differential photometry, is uncorrelated which contributes to the diagonal elements of the covariance matrix. As a result of these processing and modeling we could determine the transit parameters of the planets more accurately than the previously published results. We have adopted the stellar parameters such as mass, radius and effective temperature of the host stars and the semi-amplitude of the oscillation of the radial velocity of the host stars due to the planets (K_{RV}) from existing data available in the literature (Collier Cameron et al. 2010; Gillon et al. 2011; Bakos et al. 2012; Lehmann et al. 2015; Penev et al. 2016; Collins et al. 2017).

The paper is organized in the following way: In section-2 we discuss the details of the observations and the additional data adopted from the literature. In section-3 we outline our newly developed pipeline used for data reduction and analysis on the raw images that produce the transit light curves that are fitted with transit models. In section-4 we elaborate the preprocessing method employed that reduces the fluctuations due to the contributions by various sources of noise to the transit light curves. In Section-5 we present the results for the observations of the stars without planetary transit and discuss their utility in characterizing the stability of the baselines of the transit light curves. In Section-6 we discuss the results and the work is summarized and concluded in section-7

2. DETAILS OF OBSERVATIONS AND DATA ADOPTED FROM LITERATURE

We observed the transit events by using the 2-meter Himalayan Chandra Telescope (HCT) at Indian Astronomical Observatory (IAO), Hanle and the 1.3-meter Jagadish Chandra Bhattacharyya Telescope (JCBT) at Vainu Bappu Observatory (VBO), Kavalur. For HCT we used the back-end instrument Hanle Faint Object Spectroscopic Camera (HFOSC) which has a $2K \times 2k$ optical CCD as the imager with a field of view of $10' \times 10'$ on-sky. In case of JCBT we used the $2k \times 4k$ UKATC optical CCD as the imager with a field of view of $10' \times 20'$ on-sky. Bessel V, R and I filters were used for the observations. Both the imagers have a plate-scale of $3''/\text{pixel}$ and both are liquid Nitrogen cooled to make the dark noise negligible. In order to obtain multiple transit light curves, each target has been observed repeatedly. Some of the observed frames had to be discarded as they were affected by either passing cloud or due to the condensation of water on the CCD.

We have used the orbital period and the semi-amplitude of the radial velocity of the host star from the literature as mentioned in the next subsection (see Table 1). The rest of the planetary parameters are deduced by the detail analysis and modeling of the observational data.

2.1. WASP-33b

WASP 33 b is a hot jupiter that orbits around the host star HD 15082. We observed this object for 5 transit events - one from HCT in V filter on 09 Dec 2017, two from JCBT in I filter on 05 Jan 2018, 27 Jan 2018 and the other two from JCBT in V filter on 26 Dec 2018 and 06 Jan 2019. The host star is an A5 type star (Grenier et al. 1999). It has a mass of $1.495 \pm 0.031 M_{\odot}$ and a radius of $1.444 \pm 0.034 R_{\odot}$ (Collier Cameron et al. 2010). It is a δ Sct variable star with a V mag of 8.3 (Herrero et al. 2011). So, the transit light curves of WASP-33b are contaminated with the pulsations as reported by von Essen et al. (2014); Johnson et al. (2015). The effect of these pulsations on the estimation of the transit parameters is subtracted by adopting a denoising technique as explained in Sec-4. The orbital period of the planet is taken as 1.21987 ± 0.000001 days (Collier Cameron et al. 2010; von Essen et al. 2014; Johnson et al. 2015).

In order to determine the mass and hence the mean density of the planet, we have considered the semi-amplitude of the radial velocity of the star due to the planet as $K_{RV} = 304.0 \pm 20.0 \text{ms}^{-1}$ (Lehmann et al. 2015). The effective temperature of the host star is taken to be $T_{eff} = 7308 \pm 71$ K (Collier Cameron et al. 2010). From this the equilibrium temperature of the planet is determined (see section 6).

2.2. WASP-50b

We observed a total of 5 transit events of this hot jupiter by using JCBT in I filter on 26 Jan 2018, 28 Jan 2018 and 30 Jan 2018 and in R filter on 07 Jan 2019 and 11 Jan 2019. The host star has a V mag of 11.44, a mass of $0.892^{+0.080}_{-0.074} M_{\odot}$ and a radius of $0.843 \pm 0.031 R_{\odot}$ (Gillon et al. 2011). The T_{eff} and the semi-amplitude of the radial velocity of the star due to the planet (K_{RV}) are respectively 5400 ± 100 K and 256.6 ± 4.4 m/s (Gillon et al. 2011). The orbital period of the planet is taken as 1.955100 ± 0.000005 days (Gillon et al. 2011).

2.3. WASP-12b

By using JCBT, we observed a total of 5 transit events for this hot Jupiter - 3 in R-band on 03 Feb 2018, 04 Feb 2018 and 14 Feb 2018, one in I-band on 15 Feb 2018 and the other one in V-band on 04 Jan 2019. The host star has a mass, radius and T_{eff} of $1.434 \pm 0.11 M_{\odot}$, $1.657 \pm 0.046 R_{\odot}$ and 6300 ± 150 K respectively (Collins et al. 2017). The semi-amplitude of the radial velocity of the star due to the planet is $K_{RV} = 226 \pm 4.0 \text{ms}^{-1}$ (Collins et al. 2017). The orbital period of the planet is 1.09142 ± 0.00000014 days (Collins et al. 2017).

2.4. HATS-18b

HATS-18 b is a hot Jupiter that orbits around a G type star which is very similar to the Sun in terms of mass, radius and T_{eff} . We report the observations of four transit events of HATS-18 b, all by using JCBT. The observations were taken in I-band on 27 Jan 2018, 18 Feb 2018 and 06 Apr 2018 and in R-band on 08 Jan 2019. The host star has a mass, radius and T_{eff} of $1.037 \pm 0.047 M_{\odot}$, $1.020^{+0.057}_{-0.031} R_{\odot}$ and 5600 ± 120 K respectively (Penev et al. 2016). The semi-amplitude of radial velocity of the star is $K_{RV} = 415.2 \pm 10.0 \text{ms}^{-1}$ (Penev et al. 2016). The orbital period of the planet is 0.8378 ± 0.00000047 days (Penev et al. 2016).

2.5. HAT-P-36b

We observed HAT-P-36b during 4 transit events: On 15 Feb 2018 by using I filter, on 08 Apr 2018 and 06 May 2018 by using V filter in JCBT and on 20 Jun 2018 by using V filter in HCT. The host star is a G5V star with mass, radius and T_{eff} of $1.03 \pm 0.03 M_{\odot}$, $1.041 \pm 0.013 R_{\odot}$ and 5620 ± 40 K respectively (Bakos et al. 2012). This star is also very similar to the Sun in terms of mass, radius and T_{eff} . The semi-amplitude of radial velocity of the star due to the planet is $K_{RV} = 334.7 \pm 14.5 \text{ms}^{-1}$ (Bakos et al. 2012; Mancini et al. 2015). The orbital period of the planet is taken as 1.9551 ± 0.00005 days (Bakos et al. 2012; Mancini et al. 2015).

Table 1. Stellar and orbital parameters adopted from literature

Parameters	WASP-33 b	WASP-50 b	WASP-12 b	HATS-18 b	HAT-P-36 b
Host star mass, M_* (M_\odot)	1.495 ± 0.031	$0.892^{+0.08}_{-0.074}$	1.434 ± 0.11	1.037 ± 0.047	1.03 ± 0.03
Host star radius, R_* (R_\odot)	1.444 ± 0.034	0.843 ± 0.031	1.657 ± 0.046	$1.02^{+0.057}_{-0.031}$	1.041 ± 0.013
Host star T_{eff} (K)	7430 ± 100 (a)	5400 ± 100	6360 ± 140	5600 ± 120	5620 ± 40
Orbital Period, P (days)	1.21987 ± 0.000001	1.955100 ± 0.000005	$1.09142 \pm 1.4432 \times 10^{-7}$	$0.83784 \pm 4.7 \times 10^{-7}$	$1.32734683 \pm 0.00000048$
RV amplitude, K_{RV} (m/s)	304 ± 20	256.6 ± 4.4	226.4 ± 4.1	$415.210.0$	334.7 ± 14.5
Sources	Collier Cameron et al. (2010) Lehmann et al. (2015)	Gillon et al. (2011)	Collins et al. (2017)	Penev et al. (2016)	Bakos et al. (2012) Mancini et al. (2015)

NOTE—The value of each parameter is shown along with $1-\sigma$ error margin.

Table 2. Observation details and the night-dependent model parameters

Planet	Date of Observation	Telescope	Filter (Bessel)	Photometric S/N (median)	Mid-transit ephemerides, t_{cen} (BJD - TDB)	Cycle no. ^a	A	τ
WASP-33 b	09 Dec 2017	HCT	V	191.90	$2458097.30431 \pm 0.00000786$	4191	0.0060 ± 0.0001	20.0 ± 0.1
	05 Jan 2018	JCBT	I	1253.47	$2458124.14196 \pm 0.00000769$	4213	0.0017 ± 0.0001	20.0 ± 0.1
	27 Jan 2018	JCBT	I	300.29	$2458146.09962 \pm 0.00000765$	4231	0.0029 ± 0.0001	19.99 ± 0.1
	26 Dec 2019	JCBT	V	505.03	$2458479.12739 \pm 0.00000698$	4504	0.0044 ± 0.0001	19.99 ± 0.1
WASP-50 b	06 Jan 2019	JCBT	V	466.48	$2458490.10444 \pm 0.00000696$	4513	0.0039 ± 0.0001	18.99 ± 0.1
	26 Jan 2018	JCBT	I	361.93	$2458145.20327 \pm 0.00001057$	1323	0.00141 ± 0.0001	12.0 ± 0.1
	28 Jan 2018	JCBT	I	252.39	$2458147.15848 \pm 0.00001135$	1324	0.00232 ± 0.0001	13.0 ± 0.1
	30 Jan 2018	JCBT	I	1012.89	$2458149.11405 \pm 0.00000886$	1325	0.00096 ± 0.0001	10.0 ± 0.1
WASP-12 b	07 Jan 2019	JCBT	R	1139.06	$2458491.25582 \pm 0.00000783$	1500	0.00240 ± 0.00011	12.0 ± 0.1
	11 Jan 2019	JCBT	R	1086.67	$2458495.16601 \pm 0.00000811$	1502	0.00240 ± 0.00011	12.0 ± 0.1
	03 Feb 2017	JCBT	R	1318.76	$2458153.22835 \pm 0.00001885$	2754	$0.00037^{+0.0005}_{-0.0001}$	12.0 ± 0.1
	04 Feb 2018	JCBT	R	1180.83	$2458154.31975 \pm 0.00000770$	2755	0.00302 ± 0.0002	10.0 ± 0.1
HATS-18 b	14 Feb 2018	JCBT	R	1261.32	$2458164.14255 \pm 0.00002867$	2764	$0.00100^{+0.00025}_{-0.00014}$	10.0 ± 0.1
	15 Feb 2018	JCBT	I	500.50	$2458165.23478 \pm 0.00001119$	2765	$0.00293^{+0.0001}_{-0.0004}$	13.0 ± 0.1
	04 Jan 2019	JCBT	V	1085.84	$2458488.29489 \pm 0.00001192$	3646	$0.00300^{+0.0007}_{-0.0001}$	12.0 ± 0.1
	27 Jan 2018	JCBT	I	443.07	$2458146.42651 \pm 0.00000928$	1261	0.00099 ± 0.0001	12.0 ± 0.1
HAT-P-36 b	18 Feb 2018	JCBT	I	239.80	$2458168.21044 \pm 0.00000952$	1287	0.004 ± 0.0001	10.0 ± 0.1
	06 Apr 2018	JCBT	I	307.09	$2458215.12967 \pm 0.00001042$	1343	0.00599 ± 0.0001	7.0 ± 0.1
	08 Jan 2019	JCBT	R	425.84	$2458492.45583 \pm 0.00001028$	1674	0.00091 ± 0.0001	7.0 ± 0.1
HAT-P-36 b	15 Feb 2017	JCBT	I	329.09	$2458165.45507 \pm 0.00000686$	1959	0.00301 ± 0.0001	13.0 ± 0.1
	08 Apr 2018	JCBT	V	461.99	$2458217.22160 \pm 0.00000755$	1998	0.00175 ± 0.0001	12.99 ± 0.1
	06 May 2018	JCBT	V	589.10	$2458245.09464 \pm 0.00000737$	2019	0.00099 ± 0.0001	13.0 ± 0.1
	20 Jun 2018	HCT	V	1106.84	$2458290.22569 \pm 0.00000709$	2053	0.00088 ± 0.0001	13.0 ± 0.1

^a The mid-transit ephemerides (BJD-TDB) at cycle 0 for WASP-33 b, WASP-50 b, WASP-12 b, HATS-18 b, HAT-P-36 b are considered to be at 2452984.82964 (Turner et al. 2016), 2455558.61197 (Gillon et al. 2011), 2455147.4582 (Turner et al. 2016), 2457089.90598 (Penev et al. 2016) and 2455565.18167 (Mancini et al. 2015) respectively.

NOTE—The values of t_{cen} , A and τ are shown along with 1- σ error margin.

3. DATA REDUCTION, ANALYSIS AND MODELING

We have developed an automated pipeline based on Python and PyRAF to reduce, analyse and model the observed data. This pipeline performs the necessary bias and flat corrections on the raw images and then aligns those corrected images. Leveraging the moderately large field of view on-sky of the imagers we could image the target stars along with a few field stars that serves as reference stars for those targets. Subsequently, using the DAOPHOT package of PyRAF the pipeline automatically performs differential aperture photometry on the target stars and generates normalized light curves during the transit epoch. Henceforth, by a single light curve we will imply the light curve of a host star obtained on one particular night which may or may not contain a transit signal.

The light curves were denoised using wavelet denoising technique before modeling to decorrelate the patterns of variability common to all the stars in the frame but uncorrelated in time (del Ser et al. 2018). Also, to take care of the noise pattern unique to the host stars and correlated in time caused by stellar activity or pulsation etc., we have adopted Gaussian process correlated noise modeling technique during modeling to model its covariance structure and to take it into account when calculating the likelihood of the data given the model (Johnson et al. 2015; Barclay et al. 2015). The various sources of noise that causes the fluctuations in the light curves and their decorrelation or modeling techniques are discussed in details in the next section.

After denoising, we modeled the transit light curves by using the formalisms described in Mandel & Agol (2002). We have used the Markov Chain Monte Carlo (MCMC) technique employing Metropolis-Hastings algorithm (Collier Cameron et al. 2010) to fit the models with the observed light curves and thus determined the various physical parameters from the best fit. An essential parameter of the model is the orbital period which we have kept fixed at the values given in previously published results (Collier Cameron et al. 2010; Gillon et al. 2011; Bakos et al. 2012; Penev et al. 2016; Collins et al. 2017). For all the transit events we have assumed circular orbits of the planets. The free parameters for each transit model are the mid-transit ephemeris (t_{cen}), impact parameter (b), the scaled radius of the star (R_*/a), the ratio between the planetary and the stellar radius (R_p/R_*), the pre-ingress or post-egress baseline level (f_{star}) and the limb darkening coefficients (C_i). We have modeled all the observed transit light curves of a particular planet simultaneously. By modeling the light curves simultaneously we have deduced a single set of values for b , R_*/a and R_p/R_* for each planet. These parameters are the properties of the planet-star systems and hence independent of the observing conditions.

We deduced different sets of values for the limb darkening coefficients C_i for each host star for different filters. Also, for different transit events, we deduced different sets of values for t_{cen} and f_{star} from our model fit (Table-2) as these parameters depend on the nights of observations. For all the free parameters other than the limb darkening coefficients we have set uniform prior function (Gillon et al. 2011). We adopted quadratic limb darkening law which can be expressed as:

$$I/I(\mu = 1) = 1 - C_1(1 - \mu) - C_2(1 - \mu^2), \quad (1)$$

where $I/I(\mu = 1)$ denotes the intensity at any point on the disc normalized to that at the center. The initial values required to derive the limb darkening coefficients from the MCMC fit are taken from Claret & Bloemen (2011) and Gaussian priors was set on them (Johnson et al. 2015).

The MCMC generates a sample space of the best-fit values for the model parameters depending upon the number of walkers and iterations by maximizing the likelihood space of model fits to the light curve data. A Gaussian fit to the sample space then gives the required value of the parameters at 1σ error margins.

4. TREATMENT OF NOISE

The images captured from ground based telescopes are susceptible to noises generated from various sources. These noises are either common to all the objects in a frame and uncorrelated in time such as the noises caused by the fluctuations in the transparency, seeing, airmass etc. or unique to each object and correlated in time such as the the noises caused by the activity or pulsations of the host stars. In order to decorrelate the former type of noises from the light curves, a preprocessing on the light curves is essential before modeling to achieve high precision in the transit parameters estimated from modeling. However, the smoothing techniques such as Moving Average or Gaussian smoothing can not be used to suppress these noises as the smoothing process can distort the original light curves by removing the high frequency components of the transit signal itself and question the reliability of the properties derived therefrom.

On the other hand, for a non-stationary non-sinusoidal signal like a noisy transit signal, the wavelet denoising is much more efficient than a frequency-based filtering technique in terms of signal reconstruction and denoised S/N

(Barsanti & Gilmore 2011; Lagha et al. 2013). Wavelets have already been used extensively in the light curve noise analysis and filtering (Cubillos et al. 2017; Waldmann 2014). In case of transit photometry, wavelet denoising can efficiently remove the outliers, yield better MCMC posterior distributions and reduce the bias in the fitted transit parameters and their uncertainties (del Ser et al. 2018). We used the pywt package (Lee et al. 2018) and followed the same procedure as described in del Ser et al. (2018). Also, we simulated a transit light curve assuming a set of values for the transit parameters along with uncertainties in each parameter. The uncertainties in the parameters then reflect the errorbars in the simulated transit light curve. The wavelet denoising process is expected not to affect a light curve with errorbars limited by the uncertainty in the transit parameters. In fact we found that our simulated transit light curve was almost unchanged by the denoising process. This ensures that the light curves are not over-smoothed or the errorbars are not under-estimated by the denoising process.

The transit light curves with and without wavelet-denoising are shown in Figure 1, Figure 2, Figure 3, Figure 4 and in Figure 5. The values of the planetary physical parameters deduced by modeling the transit light curves preprocessed with wavelet denoising are presented in Table 3. The same without wavelet denoising process are provided in Table 4. A comparison of the results presented in the two tables implies that the wavelet denoising process improves the precision in the deduced parameters significantly. However, the wavelet denoising process can only efficiently remove the outliers and reduce the temporally uncorrelated noise. The temporally correlated noise unique to the host stars still remaining in the denoised transit light curves can not be directly decorrelated from the light curves. Instead, while modeling the light curves using MCMC, we also modeled the covariance structure of the correlated noise using the Gaussian process regression (GP) (Johnson et al. 2015; Barclay et al. 2015) whose mean function includes the transit model function (Mandel & Agol 2002) itself. This ensures that the effect of the correlated noise on the estimation of the posterior uncertainties on the fitted parameters is minimized. The diagonal elements of the covariance matrix are contributed by the errorbars in the transit light curves (photon noise plus readout noise). We have formed the correlation matrix using a Matern 3/2 kernel, given by (Johnson et al. 2015):

$$\kappa_{ij} = A^2 \left(1 + \frac{\sqrt{3}\Delta t_{ij}}{\tau}\right) \exp\left(-\frac{\sqrt{3}\Delta t_{ij}}{\tau}\right) + \delta_{ij}\sigma_i^2, \quad (2)$$

where, $\Delta t_{ij} = (t_i - t_j)$; t_i, t_j are two points of time of observation, σ_i is the uncertainty (error) in the flux values at time t_i and δ_{ij} is the Kronecker delta function. A and τ are the amplitude and the time scale of the fluctuation of a light curve due to the correlated noise and used in the MCMC for model fitting. We have kept A and τ variable for each light curve. The prior functions of A and τ are also chosen to be uniform. The prior function for A is estimated from the amplitude of fluctuation at the pre-ingress or post-egress points of time and the prior function of τ is estimated from the high frequency peaks on the Lomb-Scargle periodogram of each light curve. Besides, while modeling, we have multiplied the transit plus noise model with a baseline function to represent the systematics due to the other astrophysical noise or noise at the detector stage. By minimizing the Bayesian Information Criterion (BIC) we have chosen a one order baseline function of time for this purpose (Gillon et al. 2016).

Table 3. Physical parameters directly obtained and deduced from our differential transit photometry followed by preprocessing with WD technique and modeling.

Parameters	WASP-33 b	WASP-50 b	WASP-12 b	HATS-18 b	HAT-P-36 b
Transit model parameters					
Impact Parameter, b	0.21 ± 0.002	$0.669^{+0.018}_{-0.007}$	0.339 ± 0.0017	0.3 ± 0.001	0.25 ± 0.007
Scaled Stellar radius, R_*/a	0.28 ± 0.0008	0.133 ± 0.003	$0.333^{+0.0002}_{-0.0017}$	0.273 ± 0.0006	$0.21^{+0.003}_{-0.0002}$
Planet/Star Radius Ratio, R_p/R_*	0.1118 ± 0.0002	0.139 ± 0.0006	0.117 ± 0.0002	0.132 ± 0.0004	0.1199 ± 0.0002
Limb darkening coefficients					
Linear Term for V filter, $C1_V$	0.5 ± 0.01	–	0.42 ± 0.01	0.5 ± 0.01	0.53 ± 0.01
Quadratic Term for V filter, $C2_V$	0.2 ± 0.01	–	0.31 ± 0.01	0.2 ± 0.01	0.23 ± 0.01
Linear Term for R filter, $C1_R$	–	0.4 ± 0.01	0.3 ± 0.01	0.41 ± 0.01	–
Quadratic Term for R filter, $C2_R$	–	0.2 ± 0.01	0.3 ± 0.01	0.18 ± 0.01	–
Linear Term for I filter, $C1_I$	0.31 ± 0.01	0.3 ± 0.01	0.29 ± 0.01	0.31 ± 0.01	0.32 ± 0.01
Quadratic Term for I filter, $C2_I$	0.18 ± 0.01	0.2 ± 0.01	0.31 ± 0.01	0.21 ± 0.01	0.19 ± 0.01
Deduced parameters					
Transit Duration, T_{14} (days)	0.1189 ± 0.0005	0.0764 ± 0.0011	$0.1267^{+0.00009}_{-0.0005}$	0.081 ± 0.0001	$0.093^{+0.0016}_{-0.00007}$
Planet Radius, R_p (R_J)	1.593 ± 0.074	1.166 ± 0.043	1.937 ± 0.056	1.329 ± 0.075	1.277 ± 0.02
Scale Parameter, a/R_*	3.571 ± 0.01	7.51 ± 0.10	$3.0^{+0.016}_{-0.0019}$	3.658 ± 0.008	4.95 ± 0.042
Orbital Separation, a (AU)	0.0239 ± 0.00063	0.0293 ± 0.0013	0.0232 ± 0.00064	0.0174 ± 0.00098	0.0241 ± 0.00047
Orbital Inclination, i (degrees)	86.63 ± 0.03	84.88 ± 0.27	83.52 ± 0.03	85.29 ± 0.013	$87.13^{+0.004}_{-0.13}$
Planet Mass, M_p (M_J)	2.093 ± 0.139	1.4688 ± 0.092	1.465 ± 0.079	1.9795 ± 0.076	1.8482 ± 0.087
Planet Mean Density, ρ_p (gcm^{-3})	0.689 ± 0.074	1.325 ± 0.214	0.267 ± 0.0288	1.1169 ± 0.216	1.175 ± 0.078
Surface Gravity, $\log g_p$ (cgs)	3.275 ± 0.04	3.469 ± 0.029	2.998 ± 0.01	3.45 ± 0.013	3.476 ± 0.027
Equilibrium Temp. ^a , T_{eq} (K)	2781.70 ± 41.1	1394.84 ± 32.7	2592.6 ± 57.2	2069.48 ± 45.0	1780.97 ± 18.8

^a Assuming zero Bond albedo and full re-distribution of the incident stellar flux.

NOTE—The value of each parameter is shown along with 1- σ error margin. Also, some of the limb darkening coefficients are shown as –, which implies that no transit has been observed for that particular planet in that filter.

Table 4. Physical parameters directly obtained and deduced from our differential transit photometry followed by modeling and no preprocessing (without WD).

Parameters	WASP-33 b	WASP-50 b	WASP-12 b	HATS-18 b	HAT-P-36 b
Transit model parameters					
Impact Parameter, b	0.21 ± 0.003	$0.65^{+0.068}_{-0.005}$	0.339 ± 0.007	0.299 ± 0.019	0.247 ± 0.02
Scaled Stellar radius, R_*/a	0.28 ± 0.003	$0.133^{+0.01}_{-0.002}$	0.332 ± 0.002	0.26 ± 0.005	0.202 ± 0.004
Planet/Star Radius Ratio, R_p/R_*	0.1119 ± 0.003	0.135 ± 0.001	$0.117^{+0.002}_{-0.0002}$	$0.131^{+0.003}_{-0.0002}$	0.1199 ± 0.003
Limb darkening coefficients					
Linear Term for V filter, $C1_V$	0.5 ± 0.03	–	0.4 ± 0.04	0.48 ± 0.04	0.5 ± 0.05
Quadratic Term for V filter, $C2_V$	0.2 ± 0.03	–	0.3 ± 0.04	0.2 ± 0.05	0.2 ± 0.04
Linear Term for R filter, $C1_R$	–	0.39 ± 0.05	0.3 ± 0.05	0.4 ± 0.06	–
Quadratic Term for R filter, $C2_R$	–	0.21 ± 0.05	0.3 ± 0.05	0.21 ± 0.04	–
Linear Term for I filter, $C1_I$	0.3 ± 0.04	0.3 ± 0.06	0.29 ± 0.03	0.31 ± 0.05	0.3 ± 0.06
Quadratic Term for I filter, $C2_I$	0.2 ± 0.04	0.2 ± 0.06	0.3 ± 0.03	0.2 ± 0.05	0.2 ± 0.06
Deduced parameters					
Transit Duration, T_{14} (days)	0.1188 ± 0.0012	0.078 ± 0.003	0.1267 ± 0.0006	0.079 ± 0.0014	0.095 ± 0.0018
Planet Radius, R_p (R_J)	1.601 ± 0.057	1.144 ± 0.057	1.939 ± 0.058	1.341 ± 0.079	1.30 ± 0.03
Scale Parameter, a/R_*	3.571 ± 0.04	$7.485^{+0.1}_{-0.63}$	3.0 ± 0.019	3.724 ± 0.067	4.937 ± 0.1
Orbital Separation, a (AU)	0.0239 ± 0.00071	0.0289 ± 0.002	0.0231 ± 0.00068	0.0176 ± 0.001	0.0239 ± 0.00058
Orbital Inclination, i (degrees)	86.6 ± 0.05	$85.01^{+0.09}_{-1.01}$	$83.52^{+0.08}_{-0.16}$	85.38 ± 0.33	87.13 ± 0.23
Planet Mass, M_p (M_J)	2.093 ± 0.1404	1.4692 ± 0.092	1.465 ± 0.079	1.9794 ± 0.077	1.848 ± 0.088
Planet Mean Density, ρ_p (gcm^{-3})	0.6774 ± 0.095	1.2958 ± 0.21	0.266 ± 0.029	1.088 ± 0.217	1.042 ± 0.09
Surface Gravity, $\log g_p$ (cgs)	3.268 ± 0.037	$3.463^{+0.02}_{-0.1}$	2.99 ± 0.015	3.46 ± 0.03	3.432 ± 0.036
Equilibrium Temp. ^a , T_{eq} (K)	2784.09 ± 45.9	1404.63 ± 58.3	2596.19 ± 58.1	2052.09 ± 51.4	1789.92 ± 23.2

^a Assuming zero Bond albedo and full re-distribution of the incident stellar flux.NOTE—The value of each parameter is shown along with 1- σ error margin. Also, some of the limb darkening coefficients are shown as –, which implies that no transit has been observed for that particular planet in that filter.

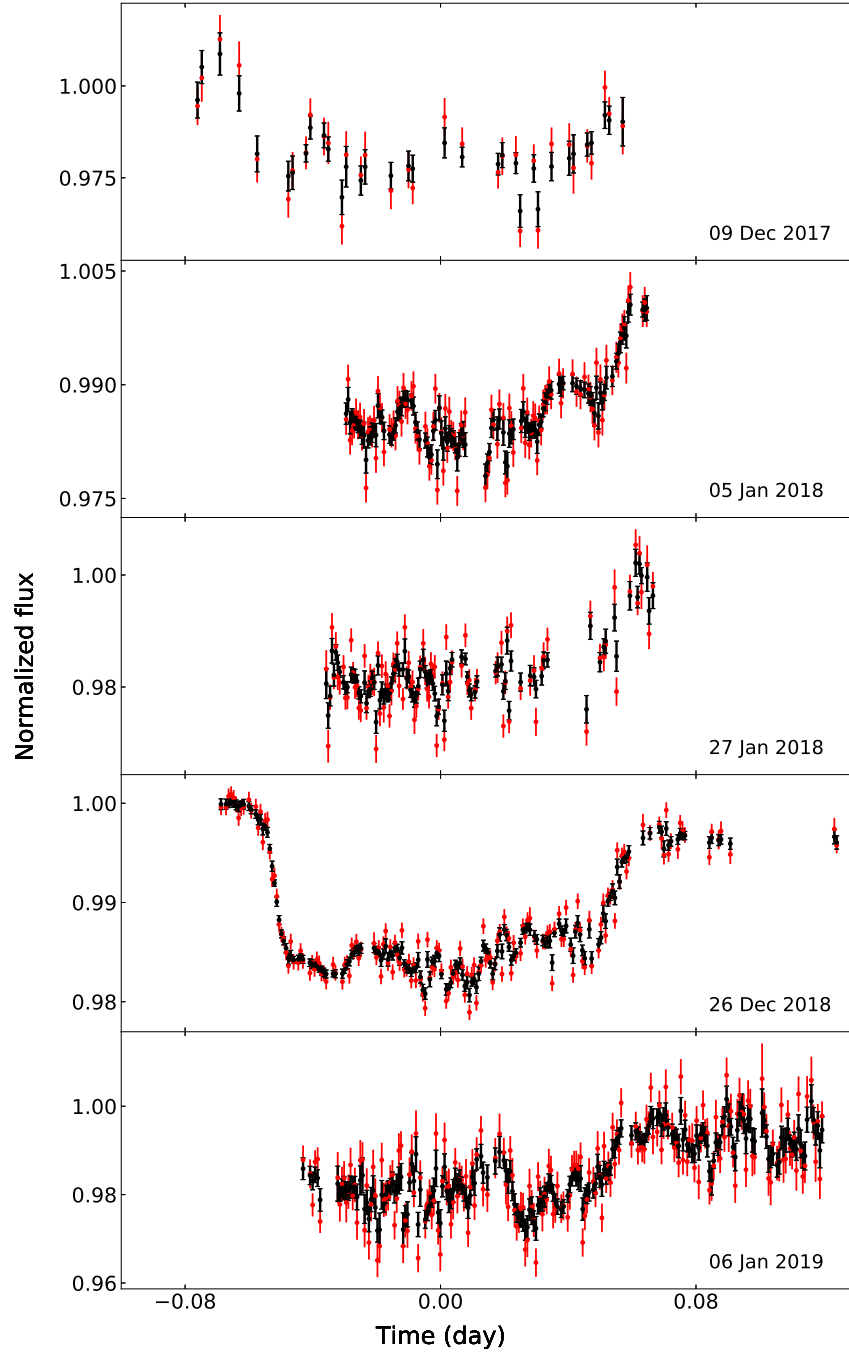


Figure 1. The transit light curves of WASP-33b. The original light curves (right after differential photometry) are shown with red errorbars and wavelet denoised light curves are over-plotted with black errorbars. The zero points on the time axes are set at the the mid-transit ephemerides as shown in Table 2.

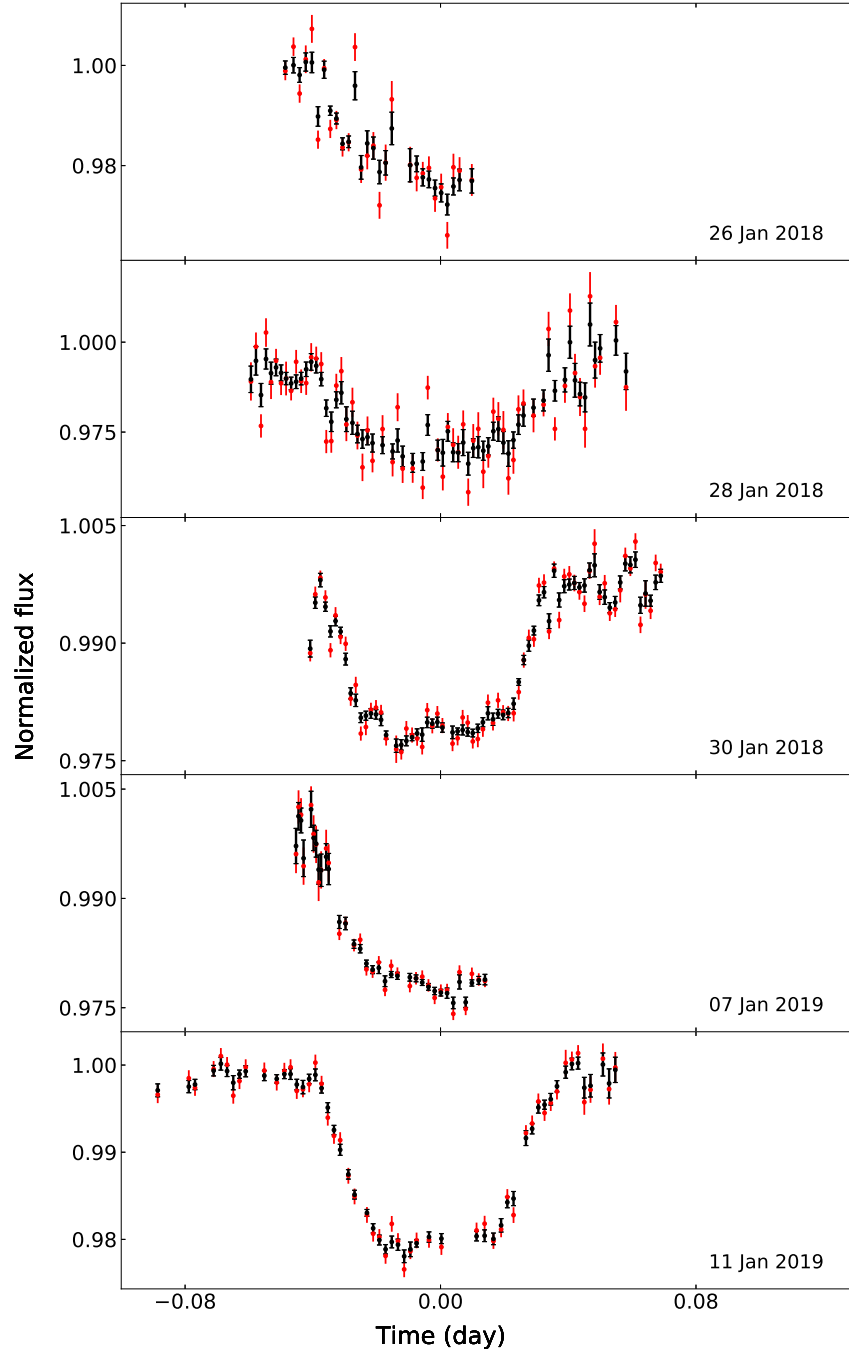


Figure 2. The transit light curves of WASP-50b. The original light curves (right after differential photometry) are shown with red errorbars and wavelet denoised light curves are over-plotted with black errorbars. The zero points on the time axes are set at the the mid-transit ephemerides as shown in Table 2.

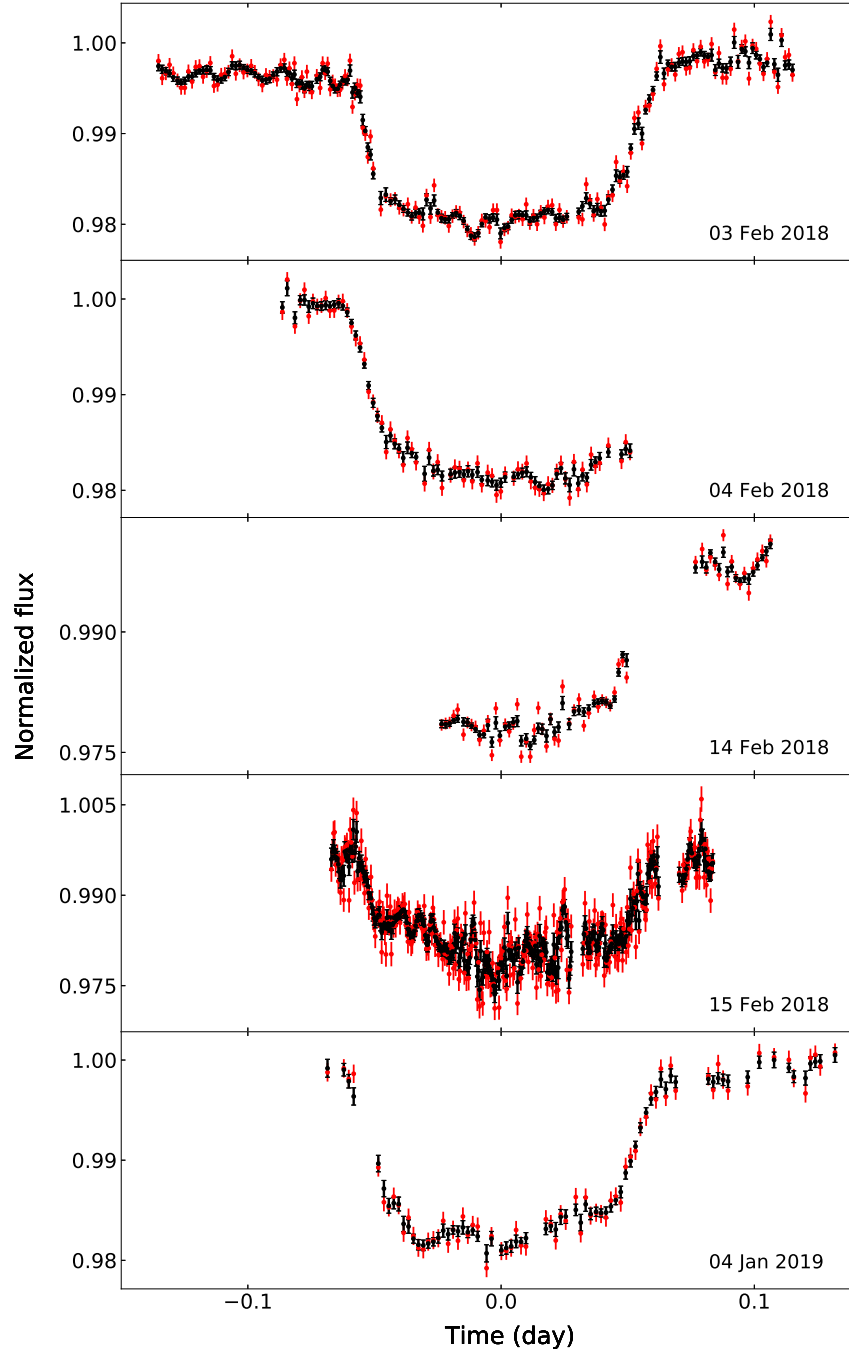


Figure 3. The transit light curves of WASP-12b. The original light curves (right after differential photometry) are shown with red errorbars and wavelet denoised light curves are over-plotted with black errorbars. The zero points on the time axes are set at the the mid-transit ephemerides as shown in Table 2.

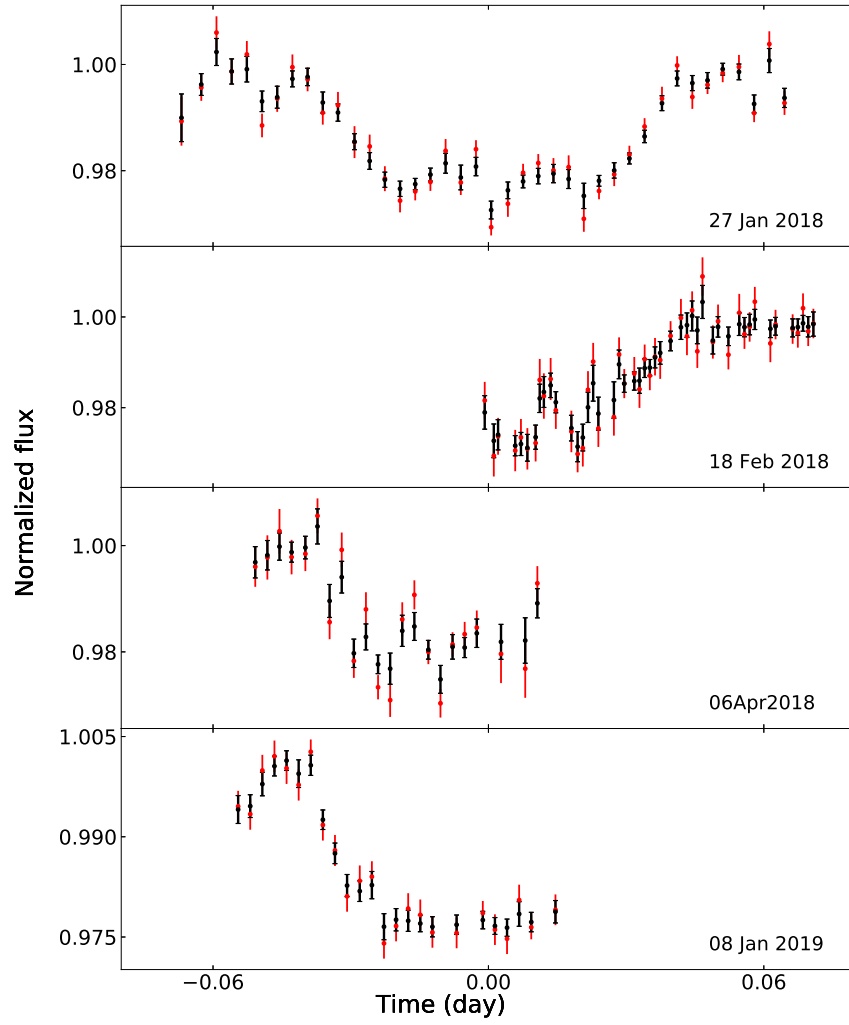


Figure 4. The transit light curves of HATS-18b. The original light curves (right after differential photometry) are shown with red errorbars and wavelet denoised light curves are over-plotted with black errorbars. The zero points on the time axes are set at the the mid-transit ephemerides as shown in Table 2.

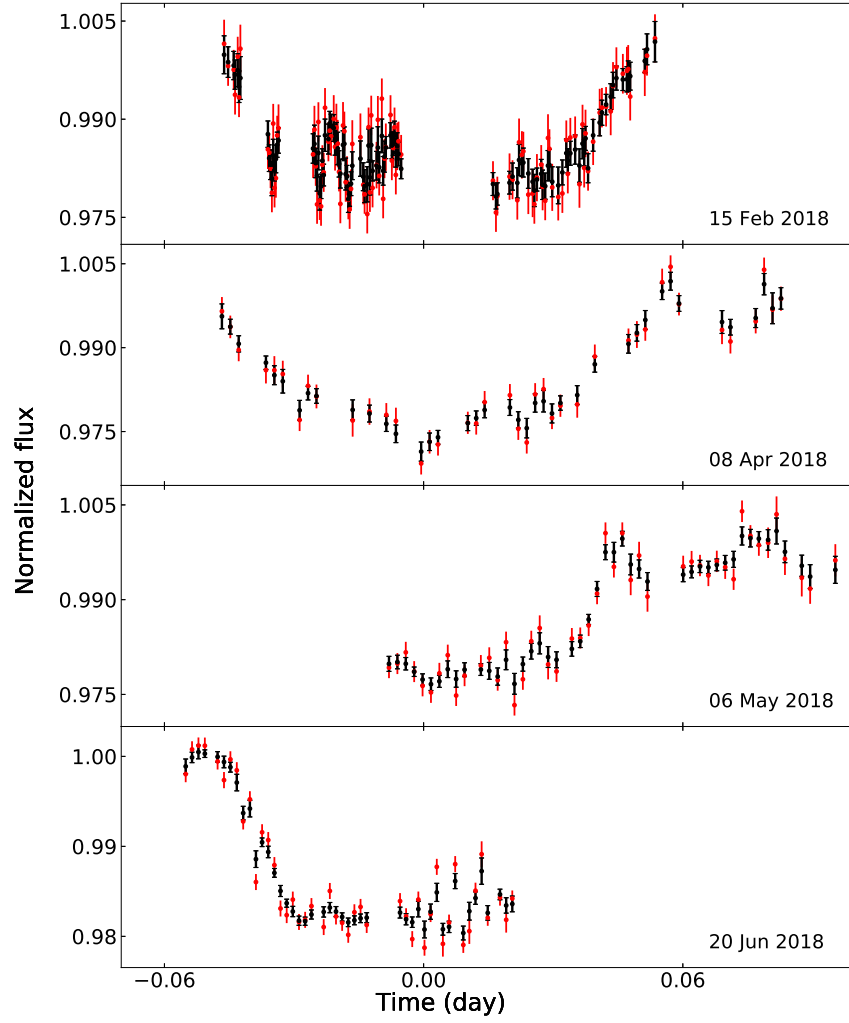


Figure 5. The transit light curves of HAT-P-36b. The original light curves (right after differential photometry) are shown with red errorbars and wavelet denoised light curves are over-plotted with black errorbars. The zero points on the time axes are set at the the mid-transit ephemerides as shown in Table 2.

5. OBSERVATIONS FOR BASELINE CHARACTERIZATION

A key element of the capability testing of the telescopes used for transit observations is the proper characterization of the baseline of the light curves that ensures the precision in the transit parameters. For this purpose, we have observed some of the host stars out of transit. Also, we monitored some fields containing multiple stars for several days which are not known to harbour any confirmed or candidate planet yet.

5.1. *Out-of-transit observations of the host stars*

In this paper we also report the results of the out-of-transit photometric observations of the host stars WASP-33 and WASP-50. We observed WASP-33 from JCBT on 10 Jan 2019 in V-band at 13:30-15 UT when there was no planetary transit. Similarly, we observed WASP-50 from JCBT on 09 Jan 2019 in R-band at 13:20-15:40 UT right before the transit by its planet. After wavelet denoising, we found a fluctuation of 0.5% in the light curve of WASP-33 which after the subtraction of the GP regression model was reduced to 0.3%. The peak signal-to-noise ratio (PSNR) was improved from about 200 to about 300 after the modeling. The light curves of WASP-50 shows a fluctuation of 0.1% which required no noise modeling because modeling does not improve it further (Table 5). The out-of-transit light curves of WASP-33 and WASP-50 during out-transit epoch are shown in Figure 6.

5.2. *Observations of stars with no known planet*

We observed the field around the star TYC 3337-1778-1. No star in this field is reported yet to have any planet. This field was neither a part of the Kepler or K2 survey nor has it been included in the list of candidates for the planet-hosting stars. We monitored this field from JCBT continuously in I-band on 05 Feb 2018 at 13:40-16:45 UT and in V-band on 04 Jan 2019 at 14:10-17:10 UT, on 05 Jan 2019 at 14:00-17:25 UT, on 06 Jan 2019 at 17:25-19:10 UT and on 08 Jan 2019 at 13:20-18:35 UT. This exercise was a part of our search program for new planets. We performed differential photometry of each target star in the field with respect to the ensemble average of a few other stars in the field to get the light curves for the target star. The temporal fluctuations in the light curves obtained for the stars in that field are not more than 0.3% and none of the light curves shows any signature of a transit event of a Jupiter-sized or Neptune-sized close-in planet within the span of our observation. However, we can not comment if any of the light curves could be attributed to a transit event of an Earth or smaller sized close-in planet or a distant (longer period) planet. We report here the light curves of 3 stars in the field namely TYC 3337-1778-1, TYC 3337-1676-1 and TYC 3337-83-1. The corresponding light curves, after wavelet denoising, are shown in Figure 7. The average fluctuations in the baselines w.r.t. the mean flux levels and the PSNR values for these stars are presented in Table 5.

Table 5. Parameters quantifying the fluctuations in the light curves with no transit signal

Date	Parameters	WASP-33 (before GP noise modeling)	WASP-33 (after GP noise modeling)	WASP-50	TYC 3337-1778-1	TYC 3337-1676-1	TYC 3337-83-1
04 Jan 2019	fluctuation (%)	–	–	–	0.12 ± 0.007	0.16 ± 0.01	0.16 ± 0.01
	PSNR	–	–	–	865 ± 55	639 ± 43	714 ± 61
05 Jan 2019	fluctuation (%)	–	–	–	0.14 ± 0.01	0.12 ± 0.009	0.16 ± 0.01
	PSNR	–	–	–	713 ± 63	872 ± 71	605 ± 40
06 Jan 2019	fluctuation (%)	–	–	–	0.15 ± 0.01	0.13 ± 0.01	0.18 ± 0.02
	PSNR	–	–	–	655 ± 70	765 ± 74	563 ± 52
08 Jan 2019	fluctuation (%)	–	–	–	0.16 ± 0.009	0.18 ± 0.007	0.26 ± 0.01
	PSNR	–	–	–	642 ± 41	552 ± 21	394 ± 22
09 Jan 2019	fluctuation (%)	–	–	0.1 ± 0.007	–	–	–
	PSNR	–	–	1119 ± 84	–	–	–
10 Jan 2019	fluctuation (%)	0.5 ± 0.05	0.3 ± 0.04	–	–	–	–
	PSNR	202 ± 19	297 ± 37	–	–	–	–

NOTE—The value of each parameter is shown along with 1- σ error margin. Also, some of the values are shown as –, which implies that no observation of that star has been made on that day.

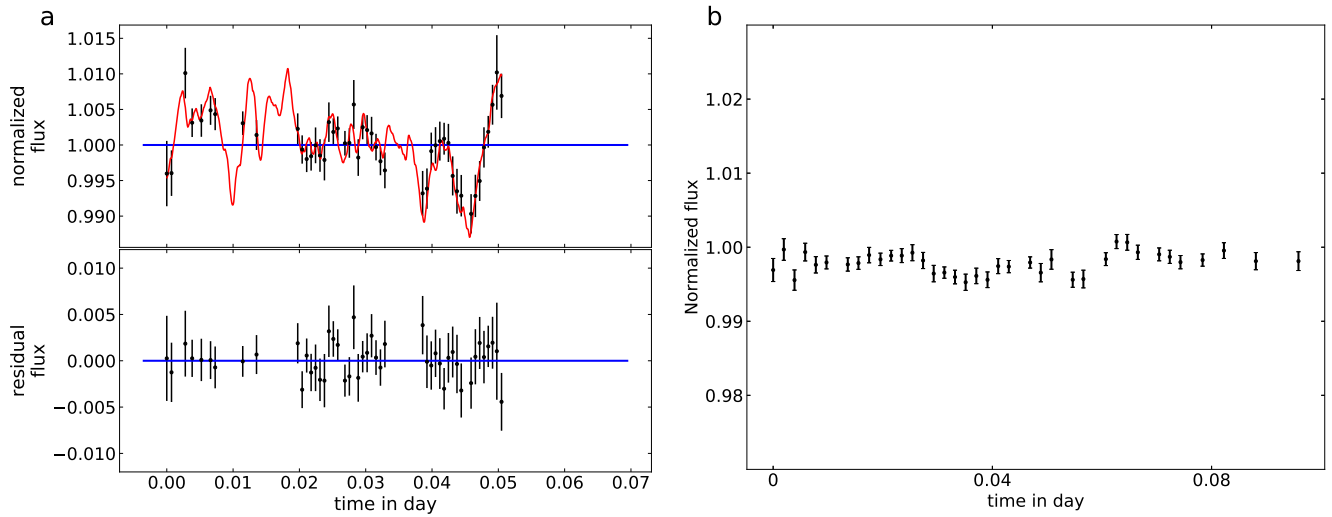


Figure 6. a - Light curve of WASP-33 observed on 10 Jan 2019 from JCBT, when there was no predicted transit event. The zero point on the time axis is set at 2458494.074141 BJD-TDB. Top- The black error-bars represent the flux and error values obtained right after wavelet denoising. The red line denotes the GP noise model. Bottom- The black error-bars represent the residual flux after subtracting the GP noise model from the wavelet denoised flux values. b - Pre-ingress wavelet denoised light curve of WASP-50 observed on 09 Jan 2019 from JCBT. The zero point on the time axis is set at 2458493.060419156 BJD-TDB. None of the plots on either side show any detectable transit signature as expected.

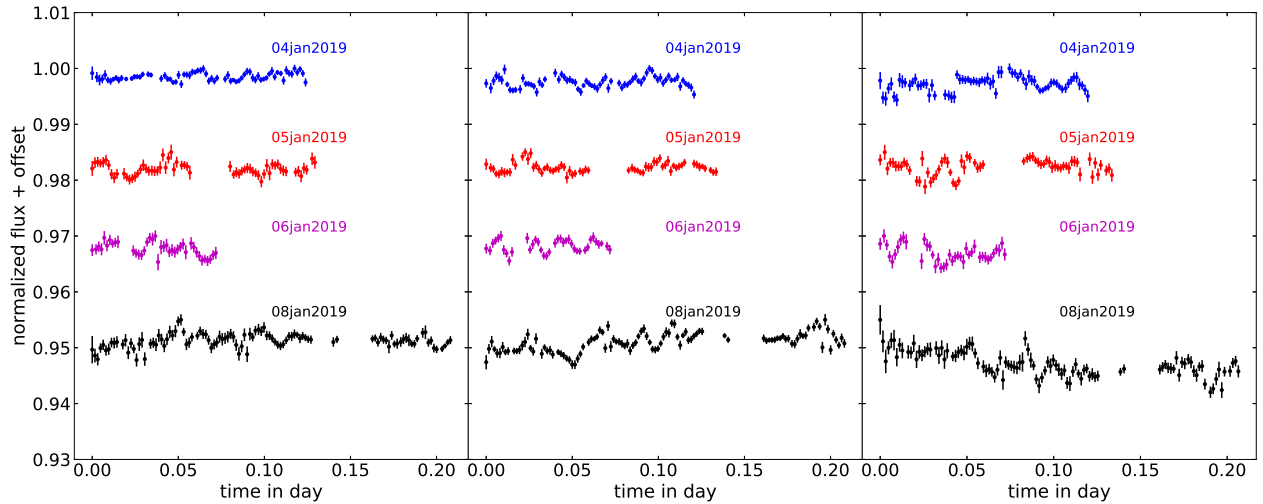


Figure 7. The light curves of the stars TYC 3337-1778-1, TYC 3337-1676-1 and TYC 3337-83-1 (from left to right) respectively observed from JCBT. The zero points on the time axes for the dates 04 Mar 2019, 05 Jan 2019, 06 Jan 2019 and 08 Mar 2019 are set at BJD-TDB 2458488.096490033, 2458489.094740324, 2458490.231318539 and 2458492.054523 respectively.

6. RESULTS AND DISCUSSION

From the search program for new planets, we have found no indication of any planetary transit event so far. However, these negative results along with the observations of the known planet-hosting stars during the out-transit epochs help us characterize the baseline stability and to calculate the lower limit of the transit depth detectable by JCBT and HCT.

Fitting the observed transit light curves with transit model by using MCMC, the physical parameters of the hot jupiters are updated with much precise values. This high precision can be attributed to the high photometric S/N and the techniques adopted to reduce the fluctuations in the light curves. Table 2 presents the median of the photometric S/N values of each light curve. The reduced transit light curves with the best fit models are shown in Figure 8, Figure 9, Figure 10, Figure 11 and in Figure 12. As evident from these figures, the fluctuations in the residual light curves are comparable or even less to the uncertainties (errors) in the flux values. As we can see from these figures, after the first stage of preprocessing i.e., WD, the light curves show different level of fluctuations for different host stars. Transit light curves for WASP-33b show maximum fluctuations due to pulsation. This is consistent with the previous observations by [von Essen et al. \(2014\)](#); [Johnson et al. \(2015\)](#). These fluctuations could be significantly reduced by GP modeling. The fluctuations in the transit light curves of WASP-50b, HATS-18b and HAT-P-36b are found to be moderate after WD and the subsequent GP noise modeling has further improved the corresponding light curves. However, the transit light curves for WASP-12b are found to show minimum fluctuations after WD and hence, WD alone would be sufficient for noise reduction in this case.

The total transit durations (T_{14}) are estimated from the model parameters using the relation as follows:

$$T_{14} = \frac{P}{\pi} \arcsin \left(\frac{\sqrt{(1 + R_p/R_*)^2 - b^2}}{\sqrt{(a/R_*)^2 - b^2}} \right) \quad (3)$$

The masses of the planets were determined by using the radial velocity of the host stars and the present updated values of the inclination angle using the relation:

$$M_p = M_*^{2/3} \left(\frac{P}{2\pi G} \right)^{1/3} \frac{K_{RV} \sqrt{1 - e^2}}{\sin i}, \quad (4)$$

using the fact that, $M_p \ll M_*$. In the absence of any observational information, we have assumed circular orbits i.e., $e = 0$. For a few targets, the orbital eccentricities have been reported to be extremely low ([Gillon et al. 2011](#); [Turner et al. 2016](#)) and therefore the assumption of circular orbit is justified.

We derived the surface gravity of the planets g_p as well by using the relation ([Southworth et al. 2007](#)):

$$\log g_p = \log \left(\frac{2\pi K_{RV} \sqrt{1 - e^2} (a/R_*)^2}{P \sin i (R_p/R_*)^2} \right) \quad (5)$$

We also estimated the equilibrium temperatures T_{eq} of the planets by assuming zero Bond albedo and full redistribution of the incident stellar flux. In term of the stellar effective temperature T_{eff} , T_{eq} can be written as

$$T_{eq} = T_{eff} \left(\frac{R_*}{2a} \right)^{1/2} \quad (6)$$

The values of M_p , T_{eq} and $\log g_p$ derived from the modeling of the transit light curves preprocessed with wavelet denoising are presented in Table-3. The same without the wavelet denoising process are presented in Table-4.

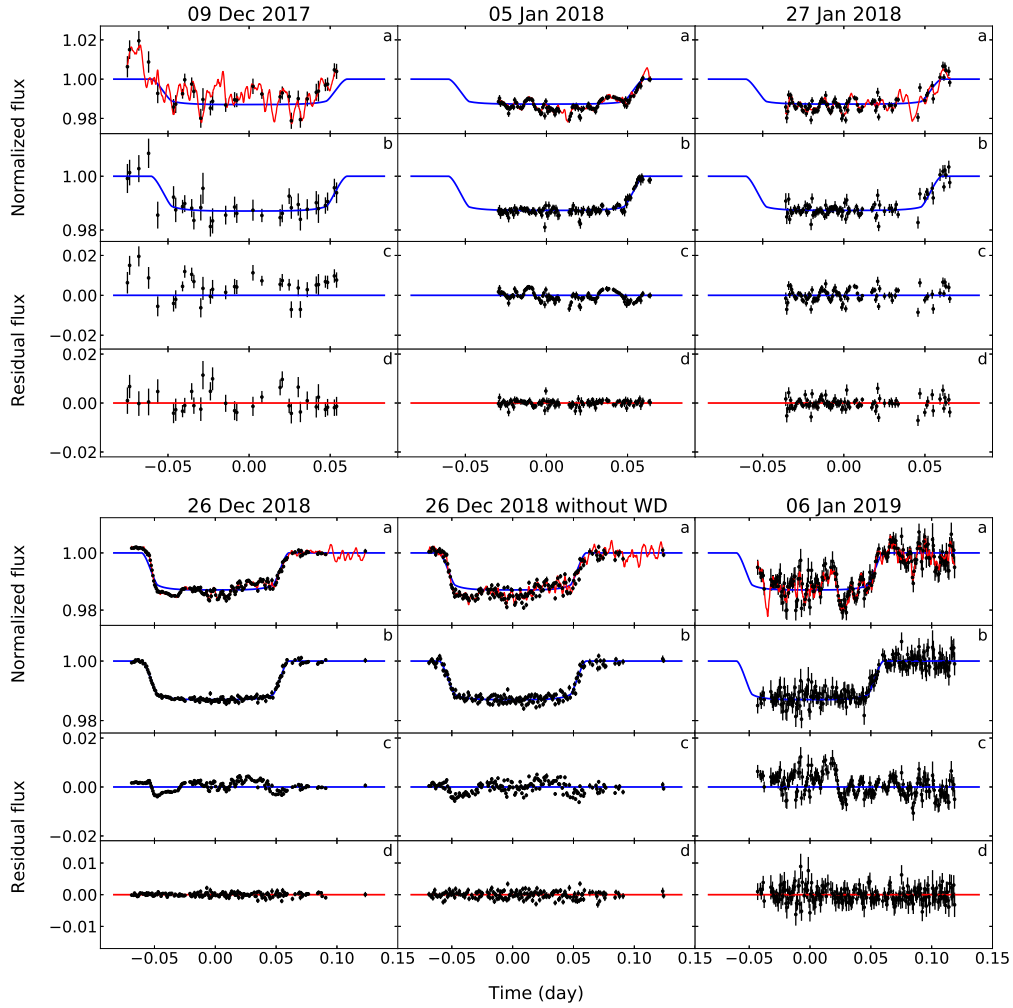


Figure 8. The normalized light curves, with and without the wavelet denoising (WD) process and the model fits for WASP-33b. The zero points on the time axes are set at the the mid-transit ephemerides as shown in Table 2.

a - The black errorbars represent the normalized wavelet-denoised flux with associated error. On top of it the MCMC-fitted transit models with and without Gaussian process correlated noise (GP) models are shown with red and blue lines respectively.

b - The black error-bars represent the normalized wavelet-denoised data minus the GP noise model. On top of it the MCMC-fitted transit models (without GP) are shown in blue lines.

c - The black error-bars represent the residual flux with error after subtracting only the transit models (without GP).

d - The black errorbars represent the residual flux plus error after subtracting both transit model and GP noise model.

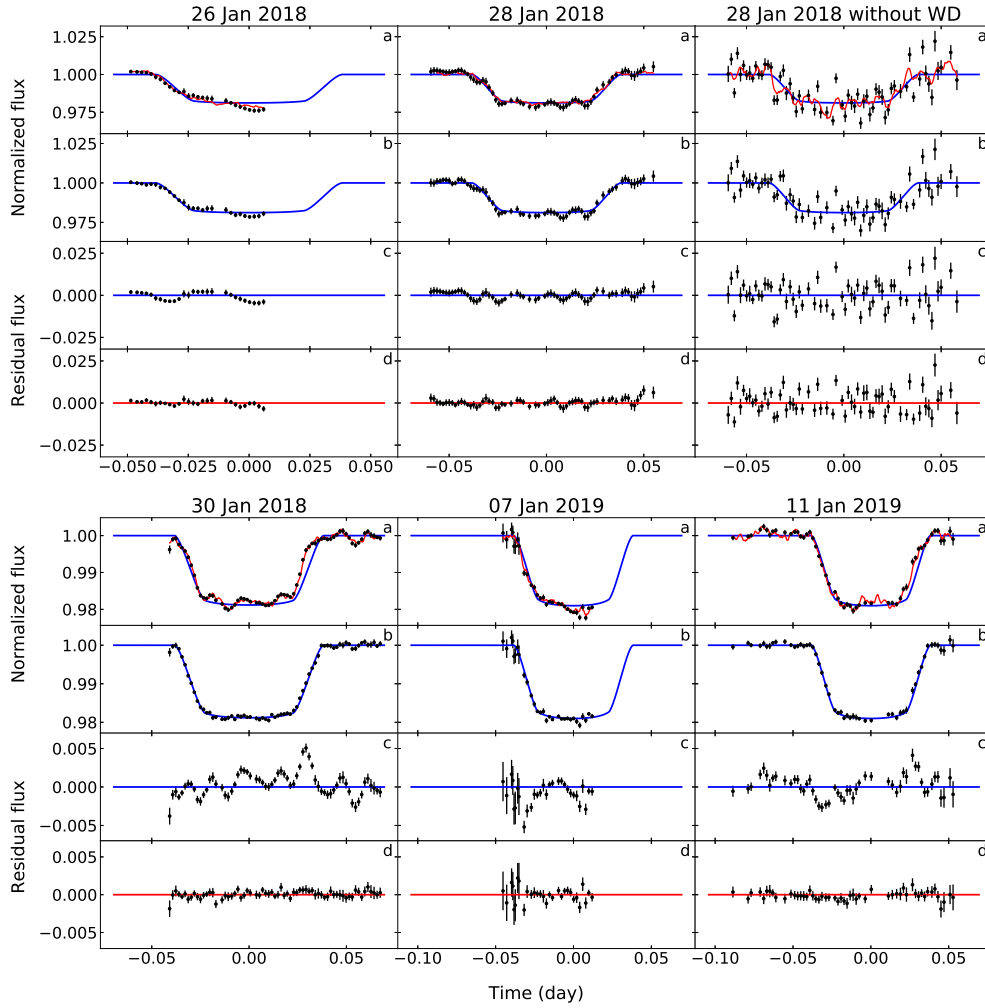


Figure 9. The normalized light curves, with and without the wavelet denoising (WD) process and the model fits for WASP-50b. The zero points on the time axes are set at the the mid-transit ephemerides as shown in Table 2.

a - The black errorbars represent the normalized wavelet-denoised flux with associated error. On top of it the MCMC-fitted transit models with and without Gaussian process correlated noise (GP) models are shown with red and blue lines respectively.

b - The black error-bars represent the normalized wavelet-denoised data minus the GP noise model. On top of it the MCMC-fitted transit models (without GP) are shown in blue lines.

c - The black error-bars represent the residual flux with error after subtracting only the transit models (without GP).

d - The black errorbars represent the residual flux plus error after subtracting both transit model and GP noise model.

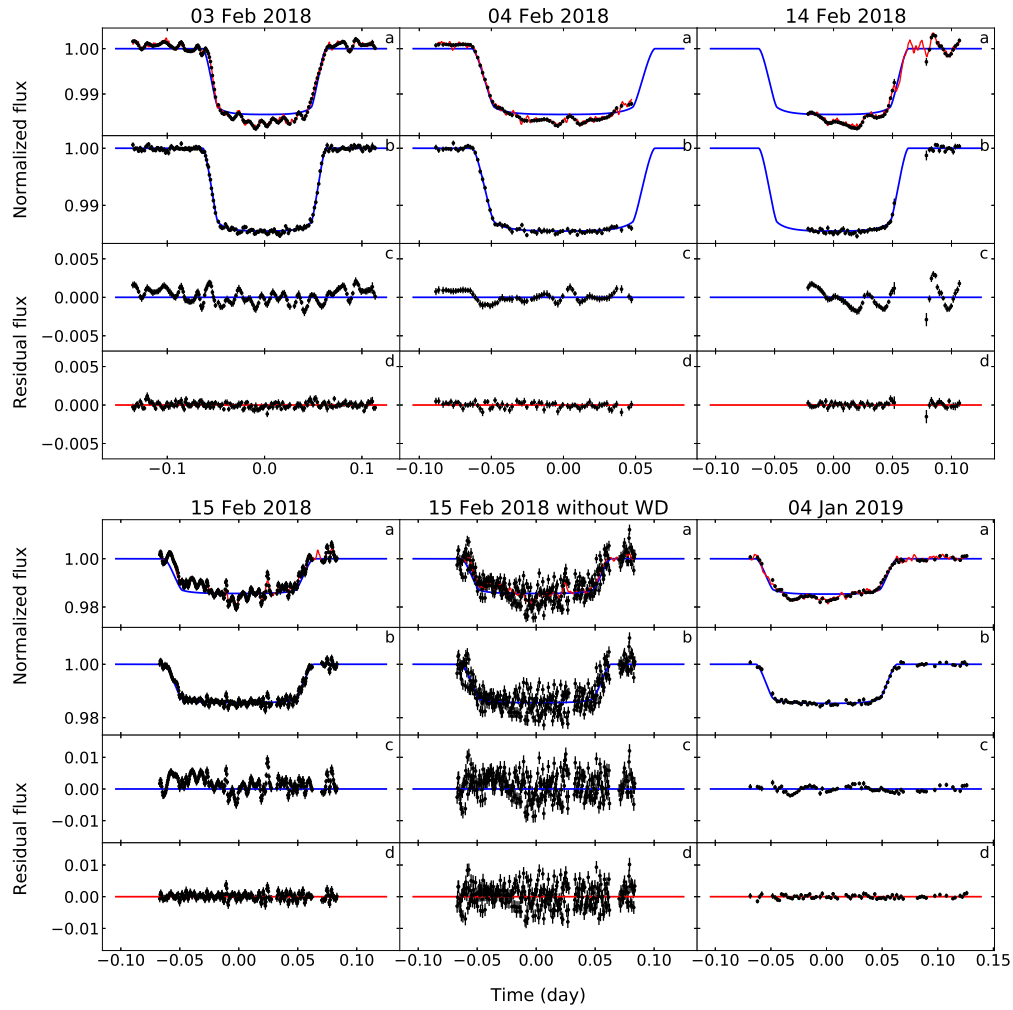


Figure 10. The normalized light curves, with and without the wavelet denoising (WD) process and the model fits for WASP-12b. The zero points on the time axes are set at the the mid-transit ephemerides as shown in Table 2.

a - The black errorbars represent the normalized wavelet-denoised flux with associated error. On top of it the MCMC-fitted transit models with and without Gaussian process correlated noise (GP) models are shown with red and blue lines respectively. b - The black error-bars represent the normalized wavelet-denoised data minus the GP noise model. On top of it the MCMC-fitted transit models (without GP) are shown in blue lines. c - The black error-bars represent the residual flux with error after subtracting only the transit models (without GP). d - The black errorbars represent the residual flux plus error after subtracting both transit model and GP noise model.

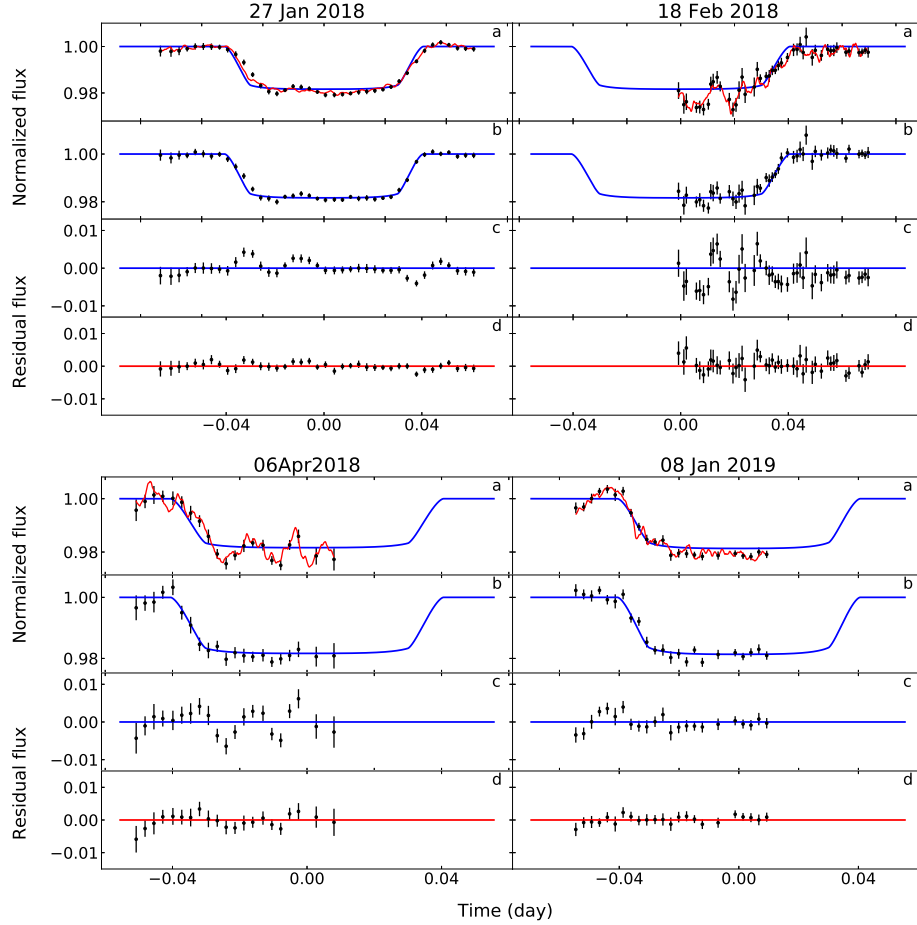


Figure 11. The normalized light curves and the model fits for HATS-18b. The zero points on the time axes are set at the the mid-transit ephemerides as shown in Table 2.

a - The black errorbars represent the normalized wavelet-denoised flux with associated error. On top of it the MCMC-fitted transit models with and without Gaussian process correlated noise (GP) models are shown with red and blue lines respectively. b - The black error-bars represent the normalized wavelet-denoised data minus the GP noise model. On top of it the MCMC-fitted transit models (without GP) are shown in blue lines. c - The black error-bars represent the residual flux with error after subtracting only the transit models (without GP). d - The black errorbars represent the residual flux plus error after subtracting both transit model and GP noise model.

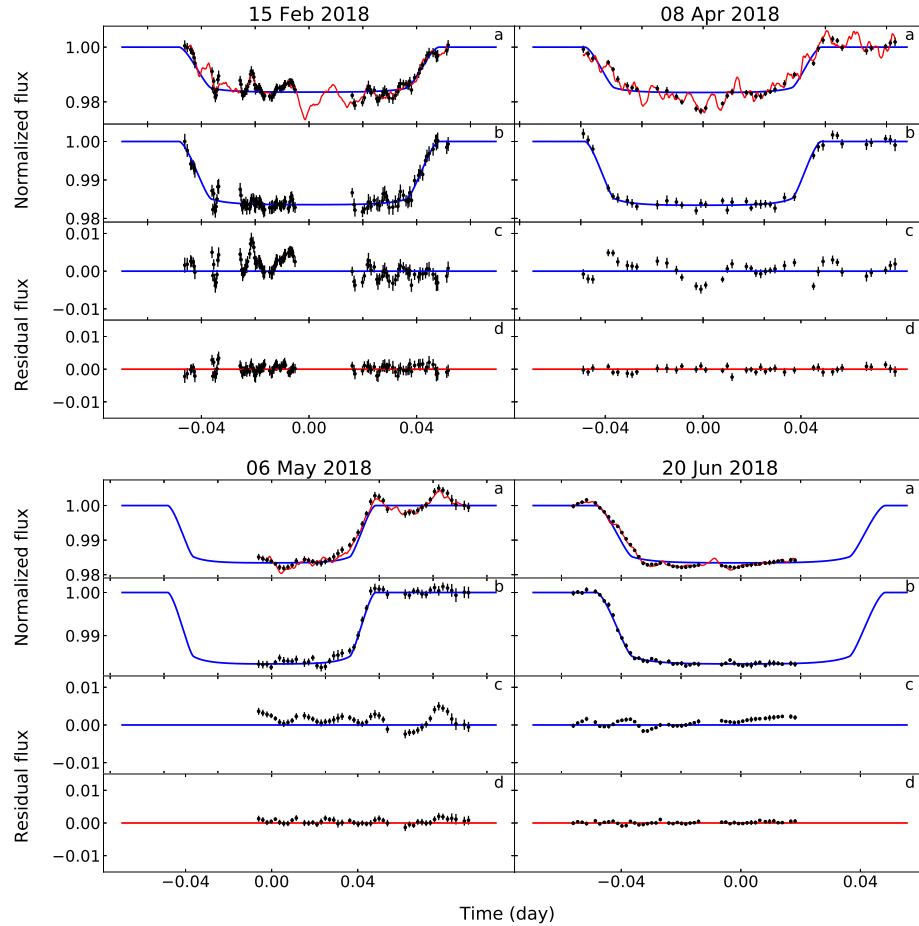


Figure 12. The normalized light curves and the model fits for HAT-P-36b. The zero points on the time axes are set at the the mid-transit ephemerides as shown in Table 2.

a - The black errorbars represent the normalized wavelet-denoised flux with associated error. On top of it the MCMC-fitted transit models with and without Gaussian process correlated noise (GP) models are shown with red and blue lines respectively. b - The black error-bars represent the normalized wavelet-denoised data minus the GP noise model. On top of it the MCMC-fitted transit models (without GP) are shown in blue lines. c - The black error-bars represent the residual flux with error after subtracting only the transit models (without GP). d - The black errorbars represent the residual flux plus error after subtracting both transit model and GP noise model.

7. CONCLUSION

We have observed the transit events of five hot Jupiters of masses ranging from $1.17 M_J$ (WASP-33b) to $1.98 M_J$ (HATS-18b) and radii ranging from $1.15 R_J$ (HAT-P-36b) to $1.82 R_J$ (WASP-12b) by using two facilities in India at different places- 1.3m JCBT and 2m HCT. We have obtained the transit light curves of these targets with very high transit S/N (transit-depth/noise). This high transit S/N can be ascribed to the high photometric S/N owing to the large apertures of the telescopes used. However, apart from the noise emanating from the stellar pulsation, we find that noise from the fluctuating sky transparency contaminates the transit signals significantly. This is a major drawback of the ground-based observations even with sufficiently large aperture of the telescope used. In the present work, we have demonstrated that wavelet denoising can efficiently suppress the uncorrelated noises to a great extent. We have also shown that the correlated noises can be estimated with high accuracy and can be subtracted from the time-series photometric data by using the Gaussian process correlated noise modeling. Thus, we could update the transit parameters of the planets with very high precision (less $1-\sigma$ error) compared to the previously published results. Hence, by combining the host star properties, the physical parameters obtained through radial velocity method and that obtained by precise transit observations, the values for the mass, radius, mean density, surface gravity etc. of the planets are obtained with improved precision.

Finally, the high stability ($\sim 500ppm$) of the light curves obtained from the observations of the stars during out-transit epoch implies that the observational facilities as well as the back-end instruments are capable of detecting the signature of planets not yet discovered.

8. ACKNOWLEDGEMENTS

We thank to the supporting staff at the Indian Astronomical Observatory (IAO), Hanle; the Centre For Research and Education in Science and Technology (CREST), Hosakote and the Vainu Bappu Observatory (VBO), Kavalur. We have used PyRAF for most of the tasks of reduction and photometry. PyRAF is a product of the Space Telescope Science Institute, which is operated by AURA for NASA. We thank K. Sankarasubramanian for his insightful inputs and M. Gillon for his help at the initial stage of this work. AC thanks C. S. Stalin, B. Kumar, S. Rakshit and D. V. S. Phanindra for their helpful suggestions. We thank the reviewer for all the useful comments.

Facilities: HCT (HFOSC), JCBT

Software: barycorr (Eastman et al. 2010), George (Ambikasaran et al. 2014), pywt (Lee et al. 2018), emcee (Foreman-Mackey et al. 2013)

REFERENCES

- Ambikasaran, S., Foreman-Mackey, D., Greengard, L., Hogg, D. W., & O’Neil, M. 2014
- Bakos, G. Á., Hartman, J. D., Torres, G., et al. 2012, *AJ*, 144, 19, doi: [10.1088/0004-6256/144/1/19](https://doi.org/10.1088/0004-6256/144/1/19)
- Barclay, T., Endl, M., Huber, D., et al. 2015, *ApJ*, 800, 46, doi: [10.1088/0004-637X/800/1/46](https://doi.org/10.1088/0004-637X/800/1/46)
- Barsanti, R. J., & Gilmore, J. 2011, in 2011 IEEE 43rd Southeastern Symposium on System Theory, 163–167
- Charbonneau, D., Brown, T. M., Latham, D. W., & Mayor, M. 2000, *ApJL*, 529, L45, doi: [10.1086/312457](https://doi.org/10.1086/312457)
- Claret, A., & Bloemen, S. 2011, *A&A*, 529, A75, doi: [10.1051/0004-6361/201116451](https://doi.org/10.1051/0004-6361/201116451)
- Collier Cameron, A., Guenther, E., Smalley, B., et al. 2010, *MNRAS*, 407, 507, doi: [10.1111/j.1365-2966.2010.16922.x](https://doi.org/10.1111/j.1365-2966.2010.16922.x)
- Collins, K. A., Kielkopf, J. F., & Stassun, K. G. 2017, *AJ*, 153, 78, doi: [10.3847/1538-3881/153/2/78](https://doi.org/10.3847/1538-3881/153/2/78)
- Cubillos, P., Harrington, J., Loredó, T. J., et al. 2017, *AJ*, 153, 3, doi: [10.3847/1538-3881/153/1/3](https://doi.org/10.3847/1538-3881/153/1/3)
- del Ser, D., Fors, O., & Núñez, J. 2018, *A&A*, 619, A86, doi: [10.1051/0004-6361/201730671](https://doi.org/10.1051/0004-6361/201730671)
- Eastman, J., Siverd, R., & Gaudi, B. S. 2010, *PASP*, 122, 935, doi: [10.1086/655938](https://doi.org/10.1086/655938)
- Foreman-Mackey, D., Hogg, D. W., Lang, D., & Goodman, J. 2013, *PASP*, 125, 306, doi: [10.1086/670067](https://doi.org/10.1086/670067)
- Gillon, M., Doyle, A. P., Lendl, M., et al. 2011, *A&A*, 533, A88, doi: [10.1051/0004-6361/201117198](https://doi.org/10.1051/0004-6361/201117198)
- Gillon, M., Jehin, E., Lederer, S. M., et al. 2016, *Nature*, 533, 221, doi: [10.1038/nature17448](https://doi.org/10.1038/nature17448)
- Grenier, S., Baylac, M.-O., Rolland, L., et al. 1999, *A&AS*, 137, 451, doi: [10.1051/aas:1999489](https://doi.org/10.1051/aas:1999489)
- Henry, G. W., Marcy, G. W., Butler, R. P., & Vogt, S. S. 2000, *ApJL*, 529, L41, doi: [10.1086/312458](https://doi.org/10.1086/312458)
- Herrero, E., Morales, J. C., Ribas, I., & Naves, R. 2011, *A&A*, 526, L10, doi: [10.1051/0004-6361/201015875](https://doi.org/10.1051/0004-6361/201015875)
- Johnson, M. C., Cochran, W. D., Collier Cameron, A., & Bayliss, D. 2015, *ApJL*, 810, L23, doi: [10.1088/2041-8205/810/2/L23](https://doi.org/10.1088/2041-8205/810/2/L23)
- Lagha, M., Tikhemirine, M., Bergheul, S., Rezoug, T., & Bettayeb, M. 2013, *Digital Signal Processing*, 23, 322, doi: [10.1016/j.dsp.2012.08.001](https://doi.org/10.1016/j.dsp.2012.08.001)
- Lee, G. R., Gommers, R., Wohlfahrt, K., et al. 2018, *PyWavelets/pywt: PyWavelets v1.0.0*, doi: [10.5281/zenodo.1407172](https://doi.org/10.5281/zenodo.1407172), <https://doi.org/10.5281/zenodo.1407172>
- Lehmann, H., Guenther, E., Sebastian, D., et al. 2015, *A&A*, 578, L4, doi: [10.1051/0004-6361/201526176](https://doi.org/10.1051/0004-6361/201526176)
- Mancini, L., Esposito, M., Covino, E., et al. 2015, *A&A*, 579, A136, doi: [10.1051/0004-6361/201526030](https://doi.org/10.1051/0004-6361/201526030)
- Mandel, K., & Agol, E. 2002, *ApJL*, 580, L171, doi: [10.1086/345520](https://doi.org/10.1086/345520)
- Penev, K., Hartman, J. D., Bakos, G. Á., et al. 2016, *AJ*, 152, 127, doi: [10.3847/0004-6256/152/5/127](https://doi.org/10.3847/0004-6256/152/5/127)
- Southworth, J., Wheatley, P. J., & Sams, G. 2007, *MNRAS*, 379, L11, doi: [10.1111/j.1745-3933.2007.00324.x](https://doi.org/10.1111/j.1745-3933.2007.00324.x)
- Turner, J. D., Pearson, K. A., Biddle, L. I., et al. 2016, *MNRAS*, 459, 789, doi: [10.1093/mnras/stw574](https://doi.org/10.1093/mnras/stw574)
- von Essen, C., Czesla, S., Wolter, U., et al. 2014, *A&A*, 561, A48, doi: [10.1051/0004-6361/201322453](https://doi.org/10.1051/0004-6361/201322453)
- Waldmann, I. P. 2014, *ApJ*, 780, 23, doi: [10.1088/0004-637X/780/1/23](https://doi.org/10.1088/0004-637X/780/1/23)